Investigating the role of dust in ice nucleation within clouds and further effects on the regional weather system over East Asia

Part II: modification of the weather system

Lin Su[1], and Jimmy C.H. Fung[2, 3]

[1] School of Science, Hong Kong University of Science and Technology, Hong Kong, China

[2] Division of Environment, Hong Kong University of Science and Technology, Hong Kong, China

[3] Department of Mathematics, Hong Kong University of Science and Technology, Hong Kong, China

Correspondence to: Lin Su (lsu@connect.ust.hk)

Keywords: East Asian dust; radiative forcing; clouds; precipitation; regional modeling

Highlights:

The direct radiative effect of dust are more pronounced than the cloud radiative effect enhanced by dust on altering the radiative budget.

The indirect effects of dust result in an increase ice clouds at mid- to upper troposphere, and a reduction of liquid clouds at low to mid-troposphere.

The total precipitation amount over East Asia remains unchanged, with the locations of the precipitation are shifted.

Abstract. An updated version of the Weather Research and Forecast model coupled with Chemistry (WRF-Chem) was applied to quantify and investigate the full effects of dust on the meteorological field over East Asia during March and April 2012. The performances of the model in simulating the short-wave and long-wave radiation, surface temperature, and precipitation over East Asia are improved by incorporating the effects of dust in the simulations. The radiative forcing induced by the direct radiative effect of dust is greater than that by the dust-enhanced cloud radiative effect. The indirect effects of dust result in a substantial increase ice clouds at mid- to upper troposphere, and a reduction in liquid clouds at low to mid-troposphere. The radiative forcing combined with the re-distribution of atmospheric water vapor results in an overall decrease of near-surface temperature and an increase of temperature at the mid- to upper troposphere over East Asia, leading to an inhibition of atmospheric instability over most land areas, but an enhancement of atmospheric instability over South China. Upon considering the effects of dust, the convective precipitation exhibits an inhibition over areas from central to East China, and an enhancement over South China. Meanwhile, the locations of non-convective precipitation are shifted due to the perturbation of cloud water path. The total amount of precipitation over East Asia remains unchanged, however, the precipitation locations are shifted. The precipitation can be enhanced or inhibited by up to 20% at particular areas.

1 Introduction

Dust is recognized as an "essential climate variable" because it is a major component of atmospheric aerosols and has significant impacts on the weather and climate system (Solomon, 2007). East Asian dust is an important contributor to global dust emissions (Ginoux et al., 2001), and thus play a significant role in affecting the regional weather system through direct effect, semi-direct and indirect effects.

Dust particles affect the radiation budget directly by absorbing, reflecting and scattering short-wave and long-wave radiation (Satheesh et al., 2006;Seinfeld et al., 2004;Lacis, 1995). The absorption of radiation by dust can further affect atmospheric static stability and surface energy budget, which may lead to an evaporation of cloud droplets. This effect is referred as semi-direct effect of dust.(Solomon, 2007). The indirect effects of dust are related to dust–cloud–interaction. (Hansen et al., 1997;Perlwitz and Miller, 2010). Dust particles are recognized as effective ice nuclei (IN) and considered to play an important role in cold cloud processes (Broadley et al., 2012;Connolly et al., 2009;Sassen, 2002), leading to the variation of the ice water content in mixed-phase and ice clouds, which further affects the formation and development of clouds, as well as precipitations (Sassen et al., 2003;Targino et al., 2006;Teller and Levin, 2006;Lohmann and Feichter, 2005).

In light of the significance of dust for the weather and climate system, assessing the effects of dust has become increasingly important. On one hand, the direct (Mallet et al., 2009;Nabat et al., 2015a;Ge et al., 2010;Hartmann et al., 2013;Huang et al., 2009;Bi et al., 2013;Liu et al., 2011a;Liu et al., 2011b;Palacios et al., 2015;Huang, 2017) and semi-direct (Tesfaye et al., 2015;Nabat et al., 2015b;Seigel et al., 2013) effects of dust has being extensively studied worldwide by applying numerical methods. On the other hand, various ice nucleation parameterizations have been implemented into global models to estimate the importance of dust in atmospheric ice nucleation (Lohmann and Diehl, 2006;Karydis et al., 2011;Hoose et al., 2008;Zhang et al., 2014), revealing that the effect of dust as IN should not be neglected in numerical models, especially in the simulations over arid regions during strong wind events (DeMott et al., 2003;Koehler et al., 2010;DeMott et al., 2015;Lohmann and Diehl, 2006;Atkinson et al., 2013). Unfortunately, , only limited work has been carried out to investigate the indirect effects of dust on the regional weather system, especially over East Asia, which is one of the major contributors to the global dust emission in the world (Ginoux et al., 2001).

59   This series of study aimed to investigate the role of East Asian dust in affecting the regional weather system. In the

60   first part of the study, The Goddard Chemistry Aerosol Radiation and Transport (GOCART) model has been coupled

61   with the aerosol-aware Thompson-Eidhammer microphysics scheme (Thompson and Eidhammer, 2014), enabling the

62   model to estimate the indirect effect of dust along with the direct and semi-direct effects, which improved the

63   simulation of the ice nucleation process involving dust particles (Su and Fung, 2017). In this work, by applying an

64   updated version of WRF-Chem, we aim to investigate the full effects of dust, including direct, semi-direct, and indirect

65   effects, on the regional weather system over East Asia during a dust-intensive period. As the semi-direct effect and

66   indirect effect of dust cannot be separated in our simulation, these two effects are merged and discussed as a part of

67   the effects of dust apart from the direct effect, and represented by "indirect effects" in the rest of the paper. This is the

68   first study to document the full effects of dust during a typical dust-intensive period over East Asia by applying an

69   online-coupled regional numerical model.

70   The remainder of the manuscript is organized as follows. The model configurations is described in Section 2, followed

71   by the model validation in Section 3. The results along with the discussion will be presented in section 4, followed by

72   the concluding remarks in Section 5.

73

74   2 Model configurations

75   The simulations were performed using an updated version of WRF-Chem based on version 3.8.1 (Grell et al., 2016).

76   The GOCART-Thompson, which is the coupling of the GOCART aerosol model and the aerosol-aware Thompson-

77   Eidhammer microphysics scheme, has been implemented in the updated WRF-Chem, to evaluate the indirect effects

78   of dust on the atmospheric ice nucleation process by serving as IN. In the GOCART-Thompson microphysics scheme,

79   the condensation and immersion freezing is parameterized by the DeMott2015 ice nucleation scheme, and two factors

80   of the DeMott2015 scheme were tuned through sensitivity experiments in the first part of this study. c_f is a calibration

81   factor in the DeMott2015 ice nucleation parameterization scheme, which was used for the nucleation of the

82   heterogeneous nucleation of ice crystals by dust particles in the GOCART-Thompson scheme, and it ranges from 1 to

83   6. According to the results of the sensitivity experiments in Part I, the calibration factor c_f was set to be 4 for the

84   simulations in this study. Furthermore, it was also demonstrated that the ice water content was still underestimated by

85   using the GOCART-Thompson scheme. To improve the simulation of the ice nucleation by dust particles, the

86 threshold relative humidity with respect to ice (RH_i) was lowered from 105% to 100% in the ice nucleation

87 parameterization, to allow the heterogeneous nucleation of ice crystals by dust particles to occur at a lower RH_i (Su

88 and Fung, 2017). Therefore, a threshold RH_i of 100% was for the simulations run with dust emissions in this study.

89 In addition, the deposition nucleation is determined by the Phillip's parameterization scheme (Phillips et al., 2008),

90 and the freezing of deliquesced aerosols using the hygroscopic aerosol concentration is parameterized following

91 Koop's parameterization scheme (Koop et al., 2000). The GOCART aerosol model was applied to simulate aerosol

92 processes (Ginoux et al., 2001;Ginoux et al., 2004) and produce ice nuclei that served by dust particles in DUST.

93 Shao's dust emission (Kang et al., 2011;Shao et al., 2011) with soil data from the United states Geological Survey

94 (Soil Survey Staff, 1993), which have been demonstrated to have good performance in reproducing dust emissions

95 over East Asia, was used to generate dust emission in the simulations of TEST. The ice nuclei were then fed into the

96 GOCART-Thompson microphysics scheme for calculating the indirect effects of dust by DeMott2015

97 parameterization scheme. In addition, the pre-given climatological profiles applied in Thompson-Eidhammer scheme

98 (Thompson and Eidhammer, 2014) were used to provide the number concentration of water-friendly aerosols for the

99 freezing of deliquesced aerosols to consider the background indirect effects of aerosols on ice nucleation for all the

100 simulations in this study.

101 Four numerical simulations were carried out to evaluate the separate effects of dust over East Asia. The configurations

102 for the four simulations are summarized in Table 1. The first simulation was termed NO-DUST/NO-CLOUD, and

103 was conducted without dust, with both the aerosol radiative feedback and cloud radiative feedback turned off. The

104 second simulation, NO-DUST/CLOUD, was also conducted without dust, with the aerosol radiative feedback turned

105 off, but the cloud radiative feedback turned on to estimate the intrinsic radiative effect of cloud. The third simulation,

106 DUST/NO-CLOUD, was conducted with the presence of dust, with the aerosol radiative feedback turned on, while

107 the cloud radiative feedback still turned off. The difference between NO-DUST/NO-CLOUD and DUST/NO-CLOUD

108 therefore represented the direct effect of dust on the radiation budget and other meteorological parameters. The last

109 simulation, DUST/CLOUD, was conducted with the presence of dust, and with both aerosol radiative feedback and

110 cloud radiative feedback turned on, to estimate the full effect of dust on the meteorological field over East Asia.

111 The important physical and chemical parameterization schemes applied for the four simulations are as follows. The

112 GOCART aerosol model was applied to simulate the aerosol processes (Ginoux et al., 2001;Ginoux et al., 2004). For

113 the dust emission simulation in DUST/NO-CLOUD and DUST/CLOUD, the Shao dust emission scheme (Shao,

114   2004;Shao et al., 2011) was applied, which had been demonstrated to closely reproduced the dust emissions over East

115   Asia (Su and Fung, 2015). Note that no aerosol emissions were considered in the simulations other than dust. The

116   Mellor–Yamada–Janjic (MYJ) turbulent kinetic energy scheme was used for the planetary boundary layer

117   parameterization (Janjić, 2002, 1994); the moisture convective processes were parameterized by the Grell–Freitas

118   scheme (Grell and Freitas, 2014); the short-wave (SW) and long-wave (LW) radiation budgets were calculated by the

119   Rapid Radiative Transfer Model for General Circulation (RRTMG) SW and LW radiation schemes (Mlawer et al.,

120   1997;Iacono et al., 2008); gravitational settling and surface deposition were combined for aerosol dry deposition

121   (Wesely, 1989); a simple washout method was used for the below-cloud wet deposition of aerosols; and the aerosol

122   optical properties were calculated based on the volume-averaging method. The newly-implemented wet scavenging

123   scheme described in Part I of this study was used for the in-cloud wet scavenging of dust particles caused by the

124   microphysical processes. As no dust was simulated in NO-DUST/NO-CLOUD and NO-DUST/CLOUD, these two

125   simulations did not included a dust emission scheme, aerosol dry and wet deposition schemes, and aerosol optical

126   schemes.

127   As described in the first part of this manuscript, two nested domains were used for all four simulations, the outer

128   domain had a horizontal resolution of 27 km, covering the entire East Asia region, and the inner domain had a

129   horizontal resolution of 9 km, covering the entire central to East China. Both domains have 40 layers, with the top

130   layer at 50 hPa. The simulation period was March 9 to April 30, 2012, with the first eight days as "spin-up" time. Only

131   the results from March 17 to April 30, 2012 were used for further analysis. Final reanalysis data provided by the

132   United States National Centre of Environmental Prediction, with a horizontal resolution of 1°, were used for generating

133   the initial and boundary conditions for the meteorological field. The simulations were re-initialized every 4 days, with

134   the aerosol field being recycled, i.e., the output of the aerosol field from the previous 4-day run was used as the initial

135   aerosol state for the next 4-day run.

136

137   **3 Model validation**

138   The simulation for dust emission was validated in Part I of this study, and the model was demonstrated to closely

139   reproduce dust emissions over East Asia during the investigated period by comparison with comprehensive

140   observational data. As this study focused on the modification of the meteorological field by the effects of dust over

141   East Asia, the capability of the model in simulating the meteorological field itself over this region requires further

142 validation.

143 The China meteorological forcing dataset (Yang et al., 2010;Chen et al., 2011) was used to assess the performance of

144 the model in reproducing the spatial distribution of the meteorological field over China. The dataset was developed

145 by the hydrometeorological research group at the Institute of Tibetan Plateau Research, Chinese Academy of Science,

146 by merging the Princeton meteorological forcing data (Sheffield et al., 2006), the Global Energy and Water Cycle

147 Experiment–Surface Radiation Budget (GEWEX-SRB) forcing data (Pinker and Laszlo, 1992), and the Global Land

148 Data Assimilation System forcing dataset (Rodell et al., 2004). The dataset contains gridded observations of the near-

149 surface temperature, precipitation rate, surface downward SW and LW radiation across China, with a spatial resolution

150 of 0.25°, dating from 1996.

151 Note that only simulation results from NO-DUST/CLOUD and DUST/CLOUD are shown, as they represent the

152 intrinsic meteorological field and the meteorological field modified by the effects of dust, respectively. For March,

153 the comparison is restricted to the observational data from March 17 to March 31, 2012, to ensure temporal overlay

154 with the corresponding simulation period. No observational data over the ocean were available, so the simulated results

155 over the ocean are also omitted to simplify the comparison.

156 The spatial distributions for the monthly average observational downward surface SW radiation for March and April

157 2012 are shown in Figure 1a and b. Overall, the SW radiation was stronger in April than in March. The SW radiation

158 was significantly higher over the West and Northwest China, due to the higher elevation of terrain over these regions,

159 and lower over East and South China, due to the lower elevation and greater cloud coverage over those regions. The

160 model closely reproduced the spatial distributions of the SW radiation in both months and accurately captured the

161 trend from March to April in the simulation results from both NO-DUST/CLOUD and DUST/CLOUD, despite a

162 certain overestimation, especially over coastal areas of East and South China. This overestimation was likely due to

163 the underestimation of clouds by the model over these areas. Compared with inland areas, cloud coverage is always

164 greater over the coastal areas of East and South China due to the abundant water vapor. Therefore, the SW radiation

165 budget over coastal areas was more sensitive to the underestimation of clouds by the model. Nevertheless, an

166 improvement in the simulation of the SW radiation budget over East Asia can be seen in the results from

167 DUST/CLOUD compared with those from NO-DUST/CLOUD. Specifically, the SW radiation produced in

168 DUST/CLOUD (Figure 1e and f) was substantially lower than that produced in NO-DUST/CLOUD (Figure 1c and d)

169 over China, especially at the dust sources and surrounding areas over the north and northwest of the country, which is

170   clearly more consistent with the observations.

171   For downward surface LW radiation, two high-value areas can be observed (Figure 2a and b). One is over Northwest

172   China, where the Taklimakan Desert is located. The strong downward LW radiation over this region was likely due

173   to the abundance of dust particles in the local atmosphere. The other area of strong LW radiation was located over

174   South China, which is warmer and contains more atmospheric water vapor. Water vapor is a potent greenhouse gas,

175   which efficiently absorbs LW radiation emitted by the Earth and heat the surrounding area, and thus increases the

176   emission of LW radiation downward (and upward) by the heated atmosphere. The model accurately simulated the

177   spatial distributions of the LW radiation over this region for both March and April in both NO-DUST/CLOUD (Figure

178   2c and d) and DUST/CLOUD (Figure 2e and f), and indeed closely captured the spatial pattern of the LW radiation

179   over China. The LW radiation over the Gobi Desert produced by DUST/CLOUD (Figure 2e and f) is slightly higher

180   than that produced by NO-DUST/CLOUD, indicating that the model reproduced the LW radiation budget more

181   accurately upon taking the effects of dust into account.

182   Similarly to the spatial distributions for the LW radiation, higher near-surface temperatures were observed over

183   Northwest China, which is a dry, arid area, and South China, which is closer to the equator (Figure 3a and b). The

184   spatial distributions of the near-surface temperature over this region were well reproduced by the model for both

185   March and April in both NO-DUST/CLOUD (Figure 3c and d) and DUST/CLOUD (Figure 3e and f). The model

186   accurately captured the spatial pattern of the surface temperature, and the two simulations did not show remarkable

187   difference in their results.

188   During the simulation period, the precipitation increased from North to South China in both months, and increased

189   from March to April over the entire region (Figure 4a and b). The spatial patterns of precipitation in March and April

190   were mostly reproduced by the model in both NO-DUST/CLOUD (Figure 4c and d) and DUST/CLOUD (Figure 4e

191   and f), but the model underestimated the precipitation in March in both simulations, especially over central and North

192   China. In April, the observed precipitation center was located over South China. Apart from underestimating the

193   precipitation over Central and North China, the NO-DUST/CLOUD simulation predicted the precipitation center to

194   be located in an area to the north of the observed center (Figure 4d), and it also underestimated the precipitation over

195   South China. In contrast, in the results of DUST/CLOUD (Figure 4f), the precipitation band to the north of South

196   China was weaker, and the precipitation over South China was slightly stronger that produced by NO-DUST/CLOUD,

197   which was more consistent with the observations.

198   The foregoing comparison of the simulation results with the observational data demonstrated that the model reasonably

199   reproduced the meteorological field over East Asia. Moreover, the meteorological field was produced more accurately

200   when the effects of dust were considered in the simulations, which consequently allows the dust-induced modification

201   of the meteorological field to be investigated.

202

203   **4 Results and discussion**

204   **4.1 Atmospheric water vapor**

205   **4.1.1 Spatial distribution**

206   The indirect effects of dust particles lead to modifications of cloud properties and cloud lifetime, and a re-distribution

207   of atmospheric water vapor. The spatial distributions of the simulated ice water path (IWP) and cloud water path

208   (CWP) from NO-DUST/CLOUD and DUST/CLOUD, as well as the difference between the two simulations

209   (DUST/CLOUD − NO-DUST/CLOUD), are presented in Figure 5. The atmospheric IWP and CWP are the column

210   sums of cloud ice water content, and cloud water content in the atmosphere per unit area. Note that the difference

211   between NO-DUST/CLOUD and DUST/CLOUD is entirely due to the full effects of dust, i.e., the direct effect of

212   dust, the cloud radiative effect enhanced by dust, and the microphysical effect of dust serving as IN in the atmosphere.

213   The spatial distributions shown in Figure 5 are the mean IWP and CWP averaged over the whole simulation period.

214   Figure 5a and b show the spatial distributions of the mean atmospheric IWP over East Asia produced from NO-

215   DUST/CLOUD and DUST/CLOUD. The IWP is concentrated over mid-latitude areas (30-40°N) in the results of NO-

216   DUST/CLOUD (Figure 5a), with values of 10-20 g/m^2. These ice crystals are mostly formed through the freezing of

217   the deliquesced water-friendly aerosols. By contrast, the IWP produced by DUST/CLOUD is substantially higher than

218   that produced by NO-DUST/CLOUD over mid-latitude areas in the simulation domain, which are the dust sources

219   and their downstream areas (Figure 5b). This corresponds to an increase by 25% to 50% over vast areas, from dust

220   source regions to the Northwest Pacific (Figure 5c), due to the dust particles serving as IN, and leading to a substantial

221   enhancement of ice crystals in the atmosphere. Dust nuclei in the atmosphere enable the super-cooled water droplets

222   to freeze into ice crystals at a much higher temperature and lower relative humidity.

223   The spatial distributions for the mean CWP over East Asia produced from NO-DUST/CLOUD and DUST/CLOUD

224   are shown in Figure 5d and e, in both of which the CWPs are concentrated over South China and the West Pacific

225   Ocean, with comparable values to each other. However, the comparison of CWPs produced from DUST/CLOUD and

226   NO-DUST/CLOUD in Figure 5f shows the existence of dust leads to a slight reduction of CWP over West, North and

227   central China, where the IWP increases substantially. Moreover, there are perturbations of CWP over East and South

228   China, as well as the West Pacific Ocean. Particularly, the CWP is generally reduced by up to 10 g/m^2 over West,

229   North and central China, and increased by up to 10 g/m2 over South China, which account for over 10% or more of

230   the total cloud water vapor at these regions.

231

232   **4.1.2 Vertical profile**

233   As the spatial distributions of IWP and CWP over East Asia are altered by the effects of dust, the cloud ice mixing

234   ratio and cloud water mixing ratio are also modified vertically. Figure 6 shows the modifications on vertical profiles

235   of the cloud ice and cloud water mixing ratios induced by the full effects of dust. Note that the vertical profiles over

236   land, over the ocean, and over the entire simulation domain for East Asia are averaged across the whole simulation

237   period.

238   Due to the effects of dust, the cloud ice mixing ratio is increased at all altitudes from the near-surface layer to higher

239   than 10 km over the whole of East Asia, as shown in Figure 6a. The cloud ice mixing ratio is uniformly increased

240   between surface to 10 km over land with a peak located at around 7km (Figure 6b), which results from the increase of

241   IN served by the abundant dust particles in the atmosphere. In contrast, the increase of the cloud ice mixing ratio over

242   the ocean is much less significant, with a higher peak located at 8-9 km (Figure 6c). A possible cause of the higher

243   peak over the ocean is that only those particles small enough to be lifted to high altitudes can be transported as far as

244   the open ocean of the West Pacific, whereas over land, more dust particles with larger sizes are suspended in lower

245   layers before settling down to the surface.

246   The vertical modification of the cloud water mixing ratio due to the effects of dust is fundamentally different from

247   that of cloud ice mixing ratio. Due to the effects of dust, the cloud water mixing ratio shows a decrease in average

248   over East Asia from surface to 7 km (Figure 6d). The overall decrease is dominated by the reduction in the cloud water

249   mixing ratio over land (Figure 6e). The cloud water mixing ratio is also decreased over the ocean near surface and

250   above 4 km, but slightly increase between 1 and 4 km (Figure 6f). The vertical modification of the cloud water mixing

251   ratio suggests that the effects of dust reduce liquid clouds at low to mid-troposphere over East Asia, especially over

252   land.

253   To summarize, the effects of dust result in a general increase of ice clouds and a slight decrease of liquid clouds over

254   East Asia as a whole, whereby the increase in cloud ice is mainly concentrated at the mid- to upper troposphere, while

255   the decrease of cloud water mostly occurs in low and mid-altitude clouds.

256   The increase in ice clouds at the mid- to upper troposphere is attributed to the indirect effects of dust. The abundant

257   IN in the atmosphere served by dust particles substantially increase the amount of ice crystals in mixed-phase and ice

258   clouds at these altitudes. In contrast, the decrease of liquid clouds at low to mid- troposphere is the result of two factors.

259   One is the warming within the atmosphere induced by the dust, leading to a much higher saturation pressure required

260   for atmospheric water vapor to form clouds, and a much faster evaporation rate of cloud droplets, which is due to the

261   cloud burning effect of dust. The other factor is that the super-cooled cloud droplets in the upper layers of the

262   troposphere freeze into ice crystals at a much higher temperature and lower relative humidity when dust particles serve

263   as IN in the atmosphere, leading to an increase of atmospheric IWP. Combined with the direct radiative effect of dust,

264   the modifications of the ice and liquid clouds induced by dust will alter the radiation budget over the region. Compared

265   to that of the increase for the ice clouds, the magnitude of the decrease for liquid clouds is smaller. However, the

266   radiative effect of liquid clouds, especially those low clouds, is much greater than that of ice clouds, therefore, the

267   decrease of liquid clouds might have a greater impact on the radiative budget over East Asia, which will be discussed

268   in the following section.

269

270   **4.2 Radiative effect**

271   The radiative effect of dust particles is demonstrated by dust-induced SW, LW, and net radiative forcing at the top of

272   the atmosphere (TOA), at the bottom of the atmosphere (BOT), and within the atmosphere (ATM). In this study, the

273   dust-induced radiative effect is represented by the difference between the SW, LW and net radiative budget produced

274   from NO-DUST/CLOUD and DUST/CLOUD, both of which output clear-sky/all-sky SW/LW radiation budget.

275   The spatial distributions for the mean radiative forcing induced by dust at the top of the atmosphere, at the bottom of

276   the atmosphere, and within the atmosphere over East Asia during the simulation period are shown in Figures 7 and 8.

277   Note that all of the spatial distributions for radiative forcing shown in the two figures are the temporal mean over the

278   entire simulation period. The SW radiative forcing was calculated as follows.

$$SW_{TOA} = SWDOWN_{TOA} - SWUP_{TOA} \qquad (1)$$

$$SW_{BOT} = SWDOWN_{BOT} - SWUP_{BOT} \qquad (2)$$

$$SW_{ATM} = SW_{TOA} + SW_{BOT} \qquad (3)$$

282 where SW_{TOA} is the SW radiative forcing at the top of the atmosphere, and SW_{BOT} is the SW radiative forcing at the

283 bottom of the atmosphere, both with positive values representing downwelling radiation; SW_{ATM} is the radiative

284 forcing within the atmosphere, which is the sum of SW_{TOA} and SW_{BOT}, with positive values representing a net

285 warming effect within the atmosphere; $SWDOWN_{TOA}$ and $SWUP_{TOA}$ are the downwelling and upwelling SW

286 radiation at the top of the atmosphere, respectively; $SWUP_{BOT}$ and $SWDOWN_{BOT}$ are the upwelling and downwelling

287 SW radiation at the bottom of the atmosphere, respectively.

288 The LW radiative forcing was calculated as follows.

289
$$LW_{TOA} = -LWUP_{TOA} \qquad (4)$$

290
$$LW_{BOT} = LWDOWN_{BOT} - LWUP_{BOT} \qquad (5)$$

291
$$LW_{ATM} = LW_{TOA} + LW_{BOT} \qquad (6)$$

292 Where LW_{TOA} is the LW radiative forcing at the top of the atmosphere, and LW_{BOT} is the LW radiative forcing at the

293 bottom of the atmosphere, both with positive values representing downwelling radiation; LW_{ATM} is the radiative

294 forcing within the atmosphere, which is the sum of LW_{TOA} and LW_{BOT}, with positive values representing warming

295 effect within the atmosphere; $LWUP_{TOA}$ is the upwelling LW radiation at the top of the atmosphere; $LWUP_{BOT}$ and

296 $LWDOWN_{BOT}$ are the upwelling and downwelling LW radiation at the bottom of the atmosphere.

297 The net radiative forcing is the sum of SW and LW radiative forcing.

298
$$Ra_{TOA} = SW_{TOA} + LW_{TOA} \qquad (7)$$

299
$$Ra_{BOT} = SW_{BOT} + LW_{BOT} \qquad (8)$$

300
$$Ra_{ATM} = SW_{ATM} + LW_{ATM} \qquad (9)$$

301

4.2.1 Clear-sky radiative forcing

303 The radiative forcing induced by dust shown in Figure 7 is also referred to as clear-sky radiative forcing, and is due

304 to the reflection, absorption and emission of radiation by dust particles suspended in the atmosphere.

305 The clear-sky downwelling SW radiation at the top of the atmosphere is slightly reduced over most land areas of East

306 Asia (Figure 7a), indicating that the upwelling SW radiation at the top of the atmosphere increases due to the reflection

307 and scattering of SW radiation by dust particles. The clear-sky SW radiative forcing at the bottom of the atmosphere

308 is negative over most of East Asia (Figure 7g), especially over dust source regions, which suggests that the solar

309 radiation that reaches the Earth's surface is substantially reduced through the absorption by dust particles suspended

310 in the atmosphere. The absorption of solar radiation by dust particles heats up the dust layers, leading to a significant

311 net warming effect within the atmosphere (Figure 7d). Averaged over the entire simulation domain, the SW radiative

312 forcing over East Asia is -0.63 W/m^2 at the top of the atmosphere, -2.19 W/m^2 at the bottom of the atmosphere, and

313 1.56 W/m^2 within the atmosphere, accounting for 0.19%, 0.87%, and 1.98% of the total clear-sky radiation budget in

314 these three zones, respectively, as shown in Table 2.

315 In Figure 7b, the clear-sky downwelling LW radiation at the top of the atmosphere is slightly increased over dust

316 source regions and downstream areas, due to the absorption of LW radiation by the thick dust layer with large fraction

317 of coarse particles in the atmosphere. In comparison, the clear-sky downwelling LW radiation is reduced at the bottom

318 of the atmosphere (Figure 7h), which is attributed to the Earth's surface being cooled as it receives less solar radiation

319 (Figure 7g). Combining the LW radiative forcing at the top of the atmosphere and at the bottom of the atmosphere,

320 there is a net negative LW radiative forcing within the atmosphere (Figure 7e). Overall, the mean LW radiative forcing

321 averaged over the entire East Asia is 0.18 W/m^2 at the top of the atmosphere, 1.44 W/m^2 at the bottom of the

322 atmosphere, and -1.94 W/m^2 within the atmosphere, accounting for 0.07%, 1.57%, and 0.74% of the total clear-sky

323 radiation budget in those three zones, respectively.

324 Combining the SW and LW radiative forcing, the net downwelling clear-sky radiation at the top of the atmosphere is

325 reduced over most of East Asia (Figure 7c). The downwelling clear-sky net radiation at the bottom of the atmosphere

326 is also reduced over most part of East Asia, especially over dust source regions and downstream areas (Figure 7i),

327 leading to a net warming effect within the atmosphere (Figure 7f), which is slightly smaller than the warming caused

328 by SW radiative forcing (Figure 7d). The net radiative forcing is -0.45 W/m^2 at the top of the atmosphere, -0.75 W/m^2

329 at the bottom of the atmosphere, and 0.30 W/m^2 within the atmosphere, accounting for 0.67%, 0.47%, and 0.33% of

330 the total clear-sky radiation budget in those three zones.

331

332 **4.2.2 All-sky radiative forcing**

333 The all-sky radiative forcing induced by dust shown in Figure 8 is the total radiative forcing, including the radiative

334 forcing directly induced by dust displayed in Figure 7, and that induced by the cloud radiative effect enhanced by dust.

335 As SW radiation is not sensitive to ice crystals in the atmosphere, the all-sky downwelling SW radiation shows a

336 smaller reduction at the top (Figure 8a) and the bottom (Figure 8g) of the atmosphere over dust sources and

337 downstream areas compared to the clear-sky case. The perturbations of all-sky SW radiation over southern part of the

338   simulation domain and the Pacific Ocean in Figure 8a and g are likely due to the fluctuation of cloud cover. Similarly,

339   the all-sky SW radiative radiation shows a warming effect within the atmosphere (Figure 8d), with an identical

340   magnitude and spatial distribution to the clear-sky case, as the warming is mostly attributed to the absorption of SW

341   radiation by dust particles. Averaged over the entire simulation domain, the mean SW radiative forcing is -0.49 W/m^2

342   at the top of the atmosphere, and –1.94 W/m^2 at the bottom of the atmosphere, and 1.44 W/m^2 within the atmosphere

343   (Table 2), accounting for 0.17%, 0.93%, and 1.81% of the total all-sky radiation budget in the three zones, respectively.

344   Compared to the clear-sky case, the positive LW radiative forcing at the top of the atmosphere is slightly increased

345   over dust sources and downstream land areas over East Asia (Figure 8b), indicating less upwelling LW radiation at

346   the top of the atmosphere. This is likely caused by the combination of the lower surface temperature due to less solar

347   radiation reaching the Earth's surface, and the absorption of LW radiation by more ice clouds induced by dust plumes

348   over these areas. The absorption of the LW radiation by more ice clouds also leads to less cooling within the

349   atmosphere (Figure 8e) compared to the clear-sky case. Moreover, a greater cloud amount results in an increase of

350   surface temperature, leading to more upwelling LW radiation emitted by the surface, and thus a smaller positive LW

351   radiative forcing at the bottom of the atmosphere (Figure 8h). As shown in Table 2, the mean all-sky LW radiative

352   forcing over the entire simulation domain is 0.31 W/m^2 at the top of the atmosphere, 1.19 W/m^2 at the bottom of the

353   atmosphere, and -1.26 W/m^2 within the atmosphere, accounting for 0.07%, 1.57%, and 0.74% of the total all-sky

354   radiation budget in the three zones, respectively.

355   Summing the SW and LW radiative forcing, the net downwelling all-sky radiation at the top of the atmosphere is

356   generally increased over dust sources, whereas reduced over the downstream land areas (Figure 8c). By contrast, the

357   net downwelling all-sky net radiation at the bottom of the atmosphere is reduced significantly over most land areas

358   over East Asia (Figure 8i). Radiative forcing results in pronounced warming within the atmosphere over East Asia as

359   a whole (Figure 8f). Averaged over the simulation domain, the net all-sky radiative forcing is -0.18 W/m^2, -0.75 W/m^2,

360   and 0.57 W/m^2 at the top of the atmosphere, at the bottom of the atmosphere, and within the atmosphere during the

361   simulation period, accounting for 0.38%, 0.56%, and 0.66% of the total net radiation budget in those three zones,

362   respectively.

363   In summary, the direct radiative effect of dust combined with the cloud radiative effect enhanced by dust generally

364   causes a net loss of radiation at the Earth's surface, but a net gain within the atmosphere, leading to a cooling at the

365   surface and lower troposphere, and a warming in mid- to upper troposphere. Nevertheless, as ice clouds enhanced by

366 dust are thin clouds, which contributes little to the modifications of both LW and SW radiation, the radiative forcing

367 induced by the indirect effects of dust is much less significant than that by the direct radiative effect of dust, therefore,

368 the dust-induced radiative forcing over East Asia is dominated by the direct radiative effect of dust. However, the

369 perturbation of the radiation budget, especially over south part of the simulation domain and the Pacific Ocean, is

370 likely due to the fluctuation of the liquid cloud amount. On average, the radiative effect caused by the increase of ice

371 clouds compensates with that resulted from the decrease of liquid clouds, leaving comparable modifications of the net

372 radiative forcing in the clear-sky case and the all-sky case.

373

374 **4.3 Vertical temperature profile**

375 Due to the radiative forcing induced by the effects of dust, the vertical temperature profile is modified. Figure 9 shows

376 the modifications of the vertical temperature profiles resulted from the direct radiative effect of dust, the cloud

377 radiative effect enhanced by dust, and the full radiative effect of dust over East Asia, over land, and over the ocean

378 during the investigated period.

379 On average, the temperature over the simulation domain as a whole is decreased below 2 km, increased from 2 km to

380 7 km, and then decreased above 7 km (Figure 9a). The contributions of the direct radiative effect of dust and dust-

381 enhanced cloud radiative effect to the vertical temperature modification are shown in Figure 9b and c. The direct

382 radiative effect of dust (Figure 9b) results in a decrease of temperature below 3 km, and an increase from 3 km to 14

383 km. In contrast, the pattern of the vertical temperature modification caused by dust-enhanced cloud radiative effect

384 (Figure 9c) is opposite to that caused by the direct effect of dust. The temperature is increased from surface to 3 km,

385 and then decreased from 3 km to 15 km.

386 As the radiative forcing induced by dust over land differs from that over the ocean, the effects on the vertical

387 temperature profile requires further discussion. The modifications of vertical temperature profile over land induced

388 by the full effects (Figure 6d), direct effect (Figure 6e) and indirect effects (Figure 6f) of dust exhibit similar

389 distributions to those over the entire domain, but with larger magnitudes. The decrease in temperature at the lower

390 level is composed of roughly equal contributions from the direct radiative effect and the dust-enhanced cloud radiative

391 effect. The decrease in temperature at lower layers is mainly attributable to the negative SW radiative forcing at the

392 surface induced by dust, and the increase of temperature at the mid troposphere is due to the absorption of SW radiation

393 by dust plumes, and the decrease of temperature at the upper troposphere might be due to that the enhancement of ice

clouds in mid- to upper troposphere prevents the upwelling LW radiation being absorbed by those ice clouds at higher altitudes.

The modification of the vertical temperature profile over the ocean is different from that over land. The temperature is increased from surface to mid-troposphere (Figure 9g), which is contributed by two factors. One is the increase of temperature at lower layers (Figure 9i) attributed to more absorption of LW radiation and latent heat released by the enhancement of low clouds. The other is the increase of temperature at mid-troposphere (Figure 9h) caused by the absorption of SW radiation by dust plumes.

4.4 Atmospheric stability

As discussed above, the radiative forcing and the re-distribution of atmospheric water content induced by dust result in a modification of the vertical temperature profile over East Asia. The corresponding shift of the thermal energy in the atmosphere eventually lead to a modification of the atmospheric stability over this region.

The K-index (*KI*) is a metric widely used in meteorology to evaluate atmospheric stability, and is calculated with the following equation (George, 2014):

$$KI = T_{850} - T_{500} + Td_{850} - (T_{700} - Td_{700}) \qquad (10)$$

where T_{850}, T_{700}, and T_{500} are the respective temperatures at 850 hPa, 700 hPa, and 500 hPa, and Td_{850} and Td_{700} are the dew points at 850 hPa and 700 hPa. The calculation of *KI* considers the atmospheric stability as a function of the vertical temperature lapse rate, the moisture content of the lower atmosphere, and the vertical extent of the moist layer. The larger the value of *KI*, the more unstable the atmosphere. To evaluate the effect of dust on atmospheric stability, *KI* was calculated from the simulation outputs.

Figure 10 shows the spatial distributions for the mean *KI* from NO-DUST/CLOUD over East Asia during the simulation period, which represents the intrinsic average atmospheric stability free from the effects of dust, and Figure 11 shows the spatial distributions for the mean difference in *KI* between DUST/NO-CLOUD and NO-DUST/NO-CLOUD (Figure 11a), between DUST/CLOUD and NO-DUST/CLOUD (Figure 11b), and between DUST/CLOUD and NO-DUST/ CLOUD (Figure 11c). The differences represent the modification in *KI* induced by the direct radiative effect of dust in Figure 11a; the indirect effects, including cloud radiative effects and re-distribution of atmospheric water content enhanced by dust, in Figure 11b; as well as the combined effects of the previous two in Figure 11c.

As shown in Figure 10, the mean *KI* over East Asia is lower in the north and increases gradually from north to south,

422 with the highest values located over the South China Sea and Southeast Asia, and the lowest values over the Central

423 to North Pacific.

424 The contributions of the direct radiative effect of dust and the indirect effects of dust on the modification of the mean

425 *KI* are shown in Figure 11a and b. The direct radiative effect of dust is to inhibit the atmospheric instability over most

426 land areas, indicated by a decrease of the mean *KI*, as shown in Figure 11a. However, the indirect effects of dust result

427 in an opposite modification of mean *KI*, with a slight enhancement of mean *KI* over most areas of the investigated

428 domain. Upon considering the full effects of dust, the mean modification of *KI* over most land areas in East Asia is a

429 general decrease (Figure 11c). The largest decrease occurs over the dust source regions and central to East China, and

430 results from the vertical modification over land. In contrast, *KI* increases over South China and most Southern part of

431 the, due to the different effects of dust on the vertical temperature over these areas.

432 Overall, the atmosphere is stabilized over the dust source regions and central to East China, but destabilized over

433 South China and most ocean areas, due to the effects of dust.

434

4.5 Precipitation

436 The modification of atmospheric stability and the re-distribution of atmospheric water content induced by dust

437 eventually alter the precipitation over East Asia. The spatial distributions for the mean precipitation rate, including

438 total precipitation, convective precipitation, and non-convective precipitation from NO-DUST/CLOUD and

439 DUST/CLOUD, as well as the difference between the two simulations, are shown in Figure 12. Note that the

440 precipitation rate shown in Figure 12 is the mean daily precipitation rate averaged over the simulation period.

441 The spatial pattern of the mean total precipitation rate from NO-DUST/CLOUD shown in Figure 12a is generally

442 similar to that from DUST/CLOUD shown in Figure 12b. However, Figure 12c shows clearly that the precipitation is

443 modified due to the effects of dust, leading to an overall reduction of the total precipitation being reduced by as much

444 as 1 mm/day or more to the east of Central to South China, where the main precipitation area is located, while an

445 increase by up to 1 mm/day to the west. Meanwhile, the precipitation rate over South China is slightly enhanced. The

446 modifications of precipitation account for up to 20% of the total simulated precipitation rate over land areas in the

447 simulation domain.

448 The simulated convective precipitation mostly occurs over the southern part of the simulation domain, with

449 precipitation centers located over East and South China, the South China Sea, and Southeast Asia (Figure 12d and e).

450 Due to the effects of dust, convective precipitation is enhanced over South China, but inhibited over East China (Figure

451 12f). The inhibition of convective precipitation over Central to East China is likely due to the general enhancement of

452 atmospheric stability, which reduces the convective motion over this region. The greater convective precipitation over

453 South China is attributed to the more unstable atmosphere, which promotes convective motions.

454 The Non-convective precipitation mainly occurs at the western rim of the Taklimakan Desert, northeast China, Japan,

455 and the areas between 27°N and 36°N over East Asia during the simulation period. The spatial distribution of the non-

456 convective precipitation rate produced in DUST/CLOUD (Figure 12h) is similar to that produced in NO-

457 DUST/CLOUD (Figure 12g). However, Figure 12i shows that the non-convective precipitation rate is modified upon

458 considering the effects of dust. The non-convective precipitation band over Central China exhibits a shift of location,

459 with less precipitation to the east and west, while more in the middle. This is likely due to the modification of liquid

460 clouds over the same area, with less clouds to the east and west, while more in the middle (Figure 5f). Similarly, the

461 enhancement or inhibition of the non-convective precipitation over South to East China is also related with the

462 perturbation of the cloud amount over these areas. On average, the amount of non-convective precipitation is increased

463 or decreased by up to 20% at the main precipitation regions.

464 To summarize, the total amount of the precipitation over the entire investigated domain remains the same by taking

465 the effects of dust into account, however, the locations of the precipitation might be shifted, the precipitation can be

466 enhanced or inhibited by up to 20% over regions with relatively abundant precipitation during the investigated period,

467 such as Central to East China, as well as South China.

468

469 **5 Conclusions**

470 By applying the updated WRF-Chem, which is capable of evaluating indirect effects of dust along with the direct

471 effect in dust simulations, the full effects of dust, including direct radiative, cloud radiative, and indirect microphysical

472 effects, on the meteorological field over East Asia during March and April 2012 were quantified and discussed.

473 By considering the effects of dust in the simulation, the atmospheric IWP is substantially increased from West China

474 to Northwest Pacific Ocean, which are the dust sources and their downstream areas with abundant dust particles

475 available to serve as IN. By contrast, the atmospheric CWP is generally reduced over the same areas, while shows

476 perturbations over the rest of areas in East Asia. Vertically, the effects of dust result in a general increase of cloud ice

477 and decrease of cloud water over East Asia as a whole, as the increase of ice clouds is mainly concentrated at the mid-

478   to upper troposphere. However, the decrease of liquid clouds mostly occurs at low- to mid-troposphere. The increase

479   of ice clouds is due to the enhancement of ice nucleation process with abundant dust particles serving as IN. The

480   reduction in liquid clouds is attributed to two factors. One is the burning effect of dust. Dust particles in the atmosphere

481   absorb radiation and warm up the surrounding environment, leading to a much greater saturation pressure required for

482   atmospheric water vapor to form clouds, and a much faster evaporation rate of cloud droplets. The other factor is that

483   the ice nucleation process enhanced by dust facilitates the freezing of atmospheric super-cooled water droplets into

484   ice crystals.

485   For the radiative forcing induced by dust, the direct radiative effect of dust combined with the dust-enhanced cloud

486   radiative effect causes a net loss of radiation at the Earth's surface, but a net gain of radiation within the atmosphere,

487   leading to cooling at the surface and lower troposphere, and warming in the mid- to upper troposphere. The radiative

488   forcing caused by the direct radiative effect of dust is greater than that induced by the dust-enhanced cloud radiative

489   effect over land areas, as the thin ice clouds enhanced by dust particles have limited impacts on altering the radiation

490   budget.

491   The modification of clouds, including ice and liquid clouds, as well as the radiative forcing induced by dust lead to an

492   altering of the vertical temperature profile. Consequently, the atmosphere is stabilized over most land areas, but

493   destabilized over South China and most oceanic areas.

494   Convective precipitation is inhibited over South China due the enhanced atmospheric stability, while enhanced over

495   Central China, resulted from the more unstable atmosphere. The modification of cloud amount results in a shift of

496   locations of the non-convective precipitation over China. On average, the total amount of the precipitation over the

497   entire investigated domain remains the same by taking the effects of dust into account, however, the locations of the

498   precipitation might be shifted, the precipitation can be enhanced or inhibited by up to 20% over particular regions

499   with relatively abundant precipitation during the investigated period.

500

501   **Data availability.** The WRF-Chem outputs are available from the authors upon request(lsu@connect.ust.hk).

502   The China Meteorological dataset can be obtained freely from the website of from Data Assimilation and Modeling

503   Center for Tibetan Multi-spheres, Institute of Tibetan Plateau Research, Chinese Academy of Sciences

504   (http://westdc.westgis.ac.cn/data/7a35329c-c53f-4267-aa07-e0037d913a21, last access: August 3 2018).

505

506

Acknowledgement. We would like to acknowledge the principle investigators and their staff from Data Assimilation and Modeling Center for Tibetan Multi-spheres, Institute of Tibetan Plateau Research, Chinese Academy of Sciences, for provision of the China Meteorological Forcing Dataset used in this study for model validation. Lin Su would like to thank Georg Grell, Stuart McKeen, and Ravan Ahmandov from the Earth System Research Laboratory, U.S. National Oceanic and Atmospheric Administration for insightful discussions. All data used in this paper are properly cited and referred to in the reference list. All data shown in the results are available upon request. This work was supported by NSFC/RGC Grant N_HKUST631/05, NSFC-FD Grant U1033001, and the RGC Grant 16303416.

514

References

Atkinson, J. D., Murray, B. J., Woodhouse, M. T., Whale, T. F., Baustian, K. J., Carslaw, K. S., Dobbie, S., O'sullivan, D., and Malkin, T. L.: The importance of feldspar for ice nucleation by mineral dust inmixed-phase clouds, Nature, 498, 355, 2013.

Bi, J., Huang, J., Fu, Q., Ge, J., Shi, J., Zhou, T., and Zhang, W.: Field measurement of clear-sky solar irradiance in Badain Jaran Desert of Northwestern China, Journal of Quantitative Spectroscopy and Radiative Transfer, 122, 194-207, 2013.

Broadley, S., Murray, B., Herbert, R., Atkinson, J., Dobbie, S., Malkin, T., Condliffe, E., and Neve, L.: Immersion mode heterogeneous ice nucleation by an illite rich powder representative of atmospheric mineral dust, Atmospheric Chemistry and Physics, 12, 287-307, 2012.

Chen, Y., Yang, K., He, J., Qin, J., Shi, J., Du, J., and He, Q.: Improving land surface temperature modeling for dry land of China, Journal of Geophysical Research: Atmospheres, 116, 2011.

Connolly, P., Möhler, O., Field, P., Saathoff, H., Burgess, R., Choularton, T., and Gallagher, M.: Studies of heterogeneous freezing by three different desert dust samples, Atmospheric Chemistry and Physics, 9, 2805-2824, 2009.

DeMott, P. J., Sassen, K., Poellot, M. R., Baumgardner, D., Rogers, D. C., Brooks, S. D., Prenni, A. J., and Kreidenweis, S. M.: African dust aerosols as atmospheric ice nuclei, Geophysical Research Letters, 30, 2003.

DeMott, P. J., Prenni, A. J., McMeeking, G. R., Sullivan, R. C., Petters, M. D., Tobo, Y., Niemand, M., Möhler, O., Snider, J. R., and Wang, Z.: Integrating laboratory and field data to quantify the immersion freezing ice nucleation activity of mineral dust particles, Atmospheric Chemistry and Physics, 15, 393-409, 2015.

Ge, J., Su, J., Ackerman, T., Fu, Q., Huang, J., and Shi, J.: Dust aerosol optical properties retrieval and radiative forcing over northwestern China during the 2008 China‐US joint field experiment, Journal of Geophysical Research: Atmospheres, 115, 2010.

George, J. J.: Weather forecasting for aeronautics, Academic press, 2014.

Ginoux, P., Chin, M., Tegen, I., Prospero, J. M., Holben, B., Dubovik, O., and Lin, S. J.: Sources and distributions of dust aerosols simulated with the GOCART model, Journal of Geophysical Research: Atmospheres, 106, 20255-20273, 2001.

Ginoux, P., Prospero, J. M., Torres, O., and Chin, M.: Long-term simulation of global dust distribution with the GOCART model: correlation with North Atlantic Oscillation, Environmental Modelling & Software, 19, 113-128, 2004.

Grell, Ahmadov, R., Peckham, S., Wong, K., Zhang, L., McKeen, S. A., Easter, R., Fast, J. D., Gustafson, W., Ma, P. L., Singh, B., Hodzic, A., Batrth, M., Pfster, G., Wolters, S., Bella, M., Freitas, S. R., Tuccella, P., Zhang, Y., Wang, K., and Klose, M.: WRF-Chem V3. 8: A summary of status and updates, EGU General Assembly Conference Abstracts, 2016.

Grell, G. A., and Freitas, S. R.: A scale and aerosol aware stochastic convective parameterization for weather and air quality modeling, Atmos. Chem. Phys, 14, 5233-5250, 2014.

Hansen, J., Sato, M., and Ruedy, R.: Radiative forcing and climate response, Journal of Geophysical Research: Atmospheres, 102, 6831-6864, 1997.

Hartmann, D., Tank, A., and Rusticucci, M.: IPCC fifth assessment report, climate change 2013: The physical science basis, IPCC AR5, 31-39, 2013.

Hoose, C., Lohmann, U., Erdin, R., and Tegen, I.: The global influence of dust mineralogical composition on heterogeneous ice nucleation in mixed-phase clouds, Environmental Research Letters, 3, 025003, 2008.

Huang, J., Fu, Q., Su, J., Tang, Q., Minnis, P., Hu, Y., Yi, Y., and Zhao, Q.: Taklimakan dust aerosol radiative heating derived from CALIPSO observations using the Fu-Liou radiation model with CERES constraints, Atmospheric Chemistry and Physics, 9, 4011-4021, 2009.

Huang, J.: Emission, transport, and radiative effects of mineral dust from the Taklimakan and Gobi deserts: comparison of measurements and model results, Atmos. Chem. Phys, 1680, 7324, 2017.

Iacono, M. J., Delamere, J. S., Mlawer, E. J., Shephard, M. W., Clough, S. A., and Collins, W. D.: Radiative forcing by long‐lived greenhouse gases: Calculations with the AER radiative transfer models, Journal of Geophysical Research: Atmospheres, 113, 2008.

Janjić, Z. I.: The step-mountain eta coordinate model: Further developments of the convection, viscous sublayer, and turbulence closure schemes, Monthly Weather Review, 122, 927-945, 1994.

Janjić, Z. I.: Nonsingular implementation of the Mellor–Yamada level 2.5 scheme in the NCEP Meso model, NCEP office note, 437, 61, 2002.

Kang, J. Y., Yoon, S. C., Shao, Y., and Kim, S. W.: Comparison of vertical dust flux by implementing three dust

570 emission schemes in WRF/Chem, Journal of Geophysical Research: Atmospheres, 116, 2011.

571 Karydis, V., Kumar, P., Barahona, D., Sokolik, I., and Nenes, A.: On the effect of dust particles on global cloud
572 condensation nuclei and cloud droplet number, Journal of Geophysical Research: Atmospheres, 116, 2011.

573 Koehler, K., Kreidenweis, S., DeMott, P., Petters, M., Prenni, A., and Möhler, O.: Laboratory investigations of the
574 impact of mineral dust aerosol on cold cloud formation, Atmospheric Chemistry and Physics, 10, 11955-11968, 2010.

575 Koop, T., Luo, B., Tsias, A., and Peter, T.: Water activity as the determinant for homogeneous ice nucleation in aqueous
576 solutions, Nature, 406, 611-614, 2000.

577 Lacis, A.: Climate forcing, climate sensitivity, and climate response: A radiative modeling perspective on atmospheric
578 aerosols, Aerosol forcing of climate, 11-42, 1995.

579 Liu, Huang, J., Shi, G., Takamura, T., Khatri, P., Bi, J., Shi, J., Wang, T., Wang, X., and Zhang, B.: Aerosol optical
580 properties and radiative effect determined from sky-radiometer over Loess Plateau of Northwest China, Atmospheric
581 Chemistry and Physics, 11, 11455-11463, 2011a.

582 Liu, Zheng, Y., Li, Z., Flynn, C., Welton, E. J., and Cribb, M.: Transport, vertical structure and radiative properties of
583 dust events in southeast China determined from ground and space sensors, Atmospheric environment, 45, 6469-6480,
584 2011b.

585 Lohmann, U., and Feichter, J.: Global indirect aerosol effects: a review, Atmospheric Chemistry and Physics, 5, 715-
586 737, 2005.

587 Lohmann, U., and Diehl, K.: Sensitivity studies of the importance of dust ice nuclei for the indirect aerosol effect on
588 stratiform mixed-phase clouds, Journal of the Atmospheric Sciences, 63, 968-982, 2006.

589 Mallet, M., Tulet, P., Serça, D., Solmon, F., Dubovik, O., Pelon, J., Pont, V., and Thouron, O.: Impact of dust aerosols
590 on the radiative budget, surface heat fluxes, heating rate profiles and convective activity over West Africa during
591 March 2006, Atmospheric Chemistry and Physics, 9, 7143-7160, 2009.

592 Mlawer, E. J., Taubman, S. J., Brown, P. D., Iacono, M. J., and Clough, S. A.: Radiative transfer for inhomogeneous
593 atmospheres: RRTM, a validated correlated‐k model for the longwave, Journal of Geophysical Research:
594 Atmospheres, 102, 16663-16682, 1997.

595 Nabat, P., Somot, S., Mallet, M., Michou, M., Sevault, F., Driouech, F., Meloni, D., Di Sarra, A., Di Biagio, C., and
596 Formenti, P.: Dust aerosol radiative effects during summer 2012 simulated with a coupled regional aerosol–
597 atmosphere–ocean model over the Mediterranean, Atmospheric Chemistry and Physics, 15, 3303-3326, 2015a.

598 Nabat, P., Somot, S., Mallet, M., Sevault, F., Chiacchio, M., and Wild, M.: Direct and semi-direct aerosol radiative
599 effect on the Mediterranean climate variability using a coupled regional climate system model, Climate dynamics, 44,
600 1127-1155, 2015b.

601 Palacios, L., Baró, R., and Jiménez-Guerrero, P.: An on-line modelling study of the direct effect of atmospheric
602 aerosols over Europe, Física de la Tierra, 27, 155, 2015.

603 Perlwitz, J., and Miller, R. L.: Cloud cover increase with increasing aerosol absorptivity: A counterexample to the
604 conventional semidirect aerosol effect, Journal of Geophysical Research: Atmospheres, 115, 2010.

605 Phillips, V. T., DeMott, P. J., and Andronache, C.: An empirical parameterization of heterogeneous ice nucleation for
606 multiple chemical species of aerosol, Journal of the atmospheric sciences, 65, 2757-2783, 2008.

607 Pinker, R., and Laszlo, I.: Modeling surface solar irradiance for satellite applications on a global scale, Journal of
608 Applied Meteorology, 31, 194-211, 1992.

609 Rodell, M., Houser, P., Jambor, U., Gottschalck, J., Mitchell, K., Meng, C., Arsenault, K., Cosgrove, B., Radakovich,
610 J., and Bosilovich, M.: The global land data assimilation system, Bulletin of the American Meteorological Society, 85,
611 381-394, 2004.

612 Sassen, K.: Indirect climate forcing over the western US from Asian dust storms, Geophysical Research Letters, 29,
613 2002.

614 Sassen, K., DeMott, P. J., Prospero, J. M., and Poellot, M. R.: Saharan dust storms and indirect aerosol effects on
615 clouds: CRYSTAL‐FACE results, Geophysical Research Letters, 30, 2003.

616 Satheesh, S., Deepshikha, S., and Srinivasan, J.: Impact of dust aerosols on Earth‐atmosphere clear‐sky albedo and
617 its short wave radiative forcing over African and Arabian regions, International Journal of Remote Sensing, 27, 1691-
618 1706, 2006.

619 Seigel, R., Van Den Heever, S., and Saleeby, S.: Mineral dust indirect effects and cloud radiative feedbacks of a
620 simulated idealized nocturnal squall line, Atmospheric Chemistry and Physics, 13, 4467-4485, 2013.

621 Seinfeld, J. H., Carmichael, G. R., Arimoto, R., Conant, W. C., Brechtel, F. J., Bates, T. S., Cahill, T. A., Clarke, A. D.,
622 Doherty, S. J., and Flatau, P. J.: ACE-ASIA: Regional climatic and atmospheric chemical effects of Asian dust and
623 pollution, Bulletin of the American Meteorological Society, 85, 367-380, 2004.

624 Shao: Simplification of a dust emission scheme and comparison with data, Journal of Geophysical Research:

625   Atmospheres, 109, 2004.
626   Shao, Ishizuka, M., Mikami, M., and Leys, J.: Parameterization of size‑resolved dust emission and validation with
627   measurements, Journal of Geophysical Research: Atmospheres, 116, 2011.
628   Sheffield, J., Goteti, G., and Wood, E. F.: Development of a 50-year high-resolution global dataset of meteorological
629   forcings for land surface modeling, Journal of Climate, 19, 3088-3111, 2006.
630   Soil Survey Staff: Soil survey manual, 1993.
631   Solomon, S.: Climate change 2007-the physical science basis: Working group I contribution to the fourth assessment
632   report of the IPCC, Cambridge University Press, 2007.
633   Su, L., and Fung, J. C.: Sensitivities of WRF‑Chem to dust emission schemes and land surface properties in
634   simulating dust cycles during springtime over East Asia, Journal of Geophysical Research: Atmospheres, 120, 2015.
635   Targino, A. C., Krejci, R., Noone, K. J., and Glantz, P.: Single particle analysis of ice crystal residuals observed in
636   orographic wave clouds over Scandinavia during INTACC experiment, Atmospheric Chemistry and Physics, 6, 1977-
637   1990, 2006.
638   Teller, A., and Levin, Z.: The effects of aerosols on precipitation and dimensions of subtropical clouds: a sensitivity
639   study using a numerical cloud model, Atmospheric Chemistry and Physics, 6, 67-80, 2006.
640   Tesfaye, M., Tsidu, G. M., Botai, J., and Sivakumar, V.: Mineral dust aerosol distributions, its direct and semi-direct
641   effects over South Africa based on regional climate model simulation, Journal of Arid Environments, 114, 22-40, 2015.
642   Thompson, G., and Eidhammer, T.: A study of aerosol impacts on clouds and precipitation development in a large
643   winter cyclone, Journal of the Atmospheric Sciences, 71, 3636-3658, 2014.
644   Wesely, M.: Parameterization of surface resistances to gaseous dry deposition in regional-scale numerical models,
645   Atmospheric Environment (1967), 23, 1293-1304, 1989.
646   Yang, K., He, J., Tang, W., Qin, J., and Cheng, C. C.: On downward shortwave and longwave radiations over high
647   altitude regions: Observation and modeling in the Tibetan Plateau, Agricultural and Forest Meteorology, 150, 38-46,
648   2010.
649   Zhang, C., Wang, M., Morrison, H., Somerville, R. C., Zhang, K., Liu, X., and Li, J. L. F.: Investigating ice nucleation
650   in cirrus clouds with an aerosol‑enabled Multiscale Modeling Framework, Journal of Advances in Modeling Earth
651   Systems, 6, 998-1015, 2014.
652
653

682   Figure 12: Spatial distributions of the average simulated total precipitation rate (a-c), convective precipitation rate (d-

683   f), and non-convective precipitation rate (g-i) from NO-DUST/CLOUD (left panel), DUST/CLOUD (middle panel),

684   and the difference between DUST/CLOUD and NO-DUST/CLOUD (right panel).

685

686   **Table 1:** Model configurations for the numerical simulations.

Experiment / Scheme	NO-DUST/NO-CLOUD	NO-DUST/CLOUD	DUST/NO-CLOUD	DUST/CLOUD
Dust emission scheme	----	----	Shao	Shao
Dry deposition	----	----	Gravitational settling/surface deposition	Gravitational settling/surface deposition
Wet deposition	----	----	In-cloud and below-cloud	In-cloud and below-cloud
Aerosol optical scheme	----	----	Maxwell-Garnett	Maxwell-Garnett
Aerosol radiative feedback	off	off	on	on
Cloud radiative feedback	off	on	off	on

687

Table 2: WRF-Chem-simulated SW, LW, and net radiative forcing (W/m^2) induced by dust over East Asia at TOA, BOT, and ATM.

	Clear-sky			All-sky		
	SW	LW	Net	SW	LW	Net
TOA (+down)	-0.63	0.18	-0.45	-0.49	0.31	-0.18
ATM (+warm)	1.56	-1.26	0.30	1.44	-0.88	0.57
BOT (+down)	-2.19	1.44	-0.75	-1.94	1.19	-0.75

SW: short-wave radiative forcing; LW: long-wave radiative forcing; Net: net radiative forcing.
TOA: radiative forcing at the top of the atmosphere; ATM: radiative effect within the atmosphere; BOT: radiative effect at the bottom of the atmosphere.
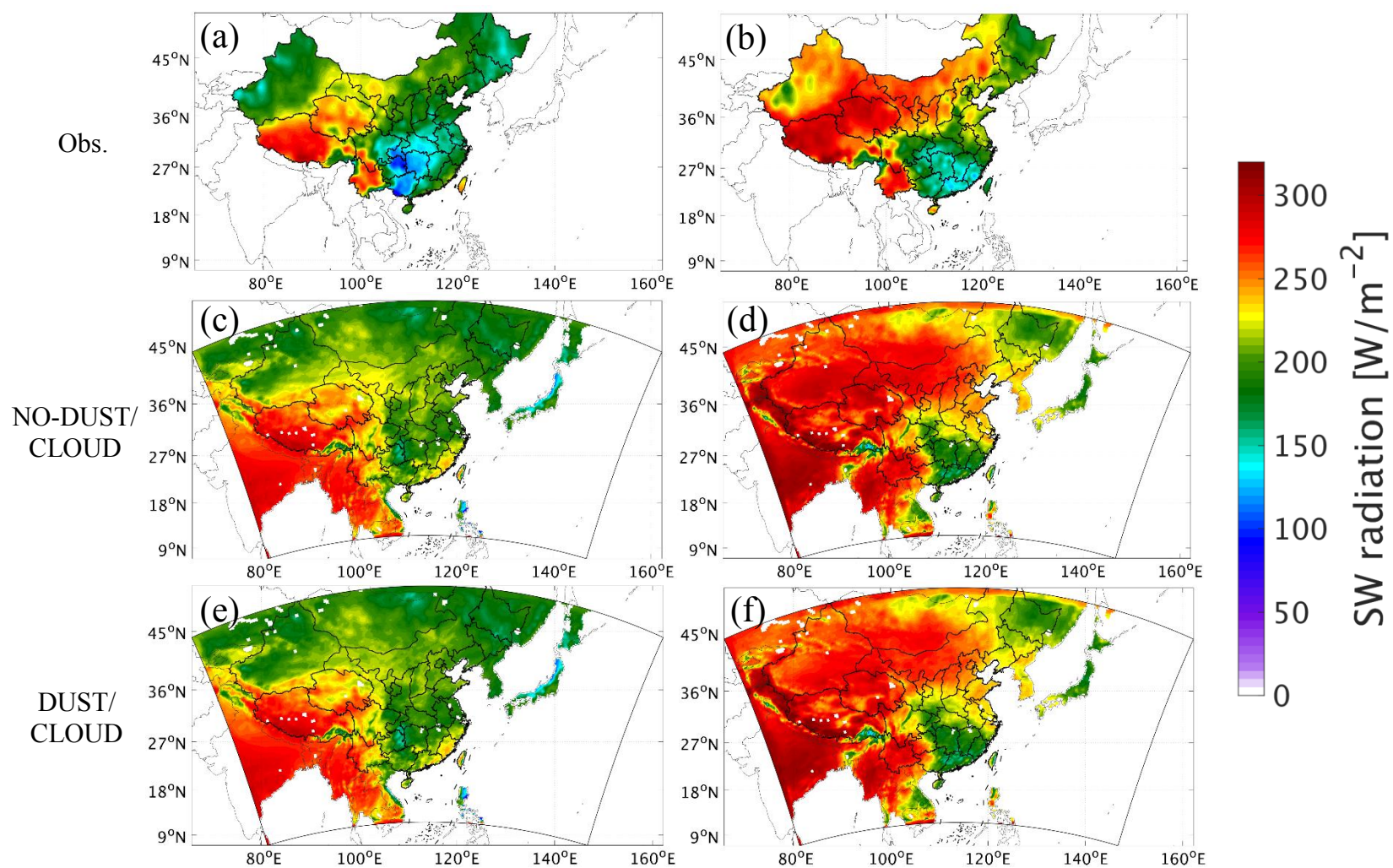
Figure 1: Spatial distributions of the average downward SW radiation at surface from observations (a, b), from NO-DUST/CLOUD (c, d), and from DUST-CLOUD (e, f) during March (left panel) and April (right panel) 2012.
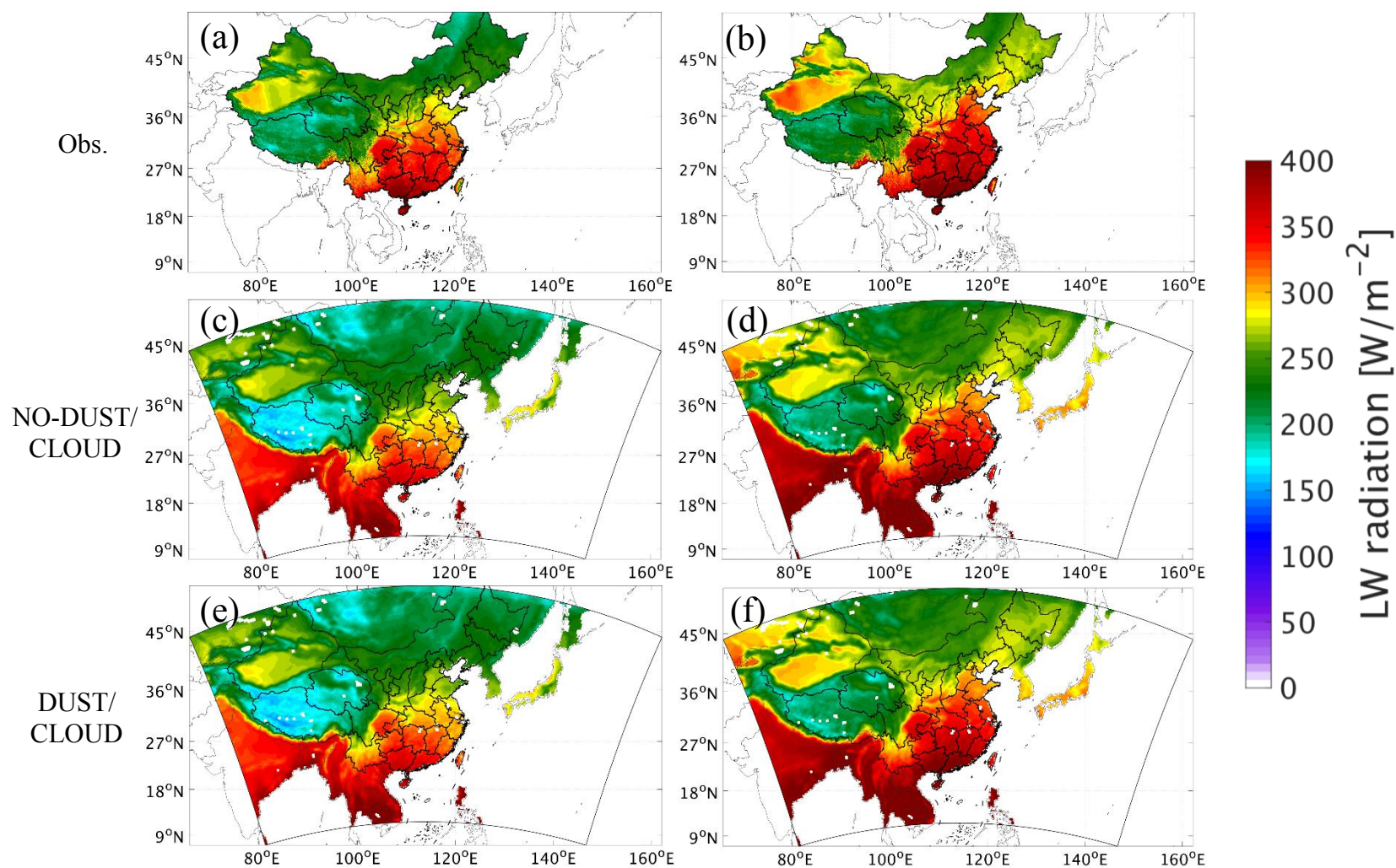
Figure 2: Spatial distributions of the average downward LW radiation at surface from observations (a, b), from NO-DUST/CLOUD (c, d), and from DUST-CLOUD (e, f) during March (left panel) and April (right panel) 2012.
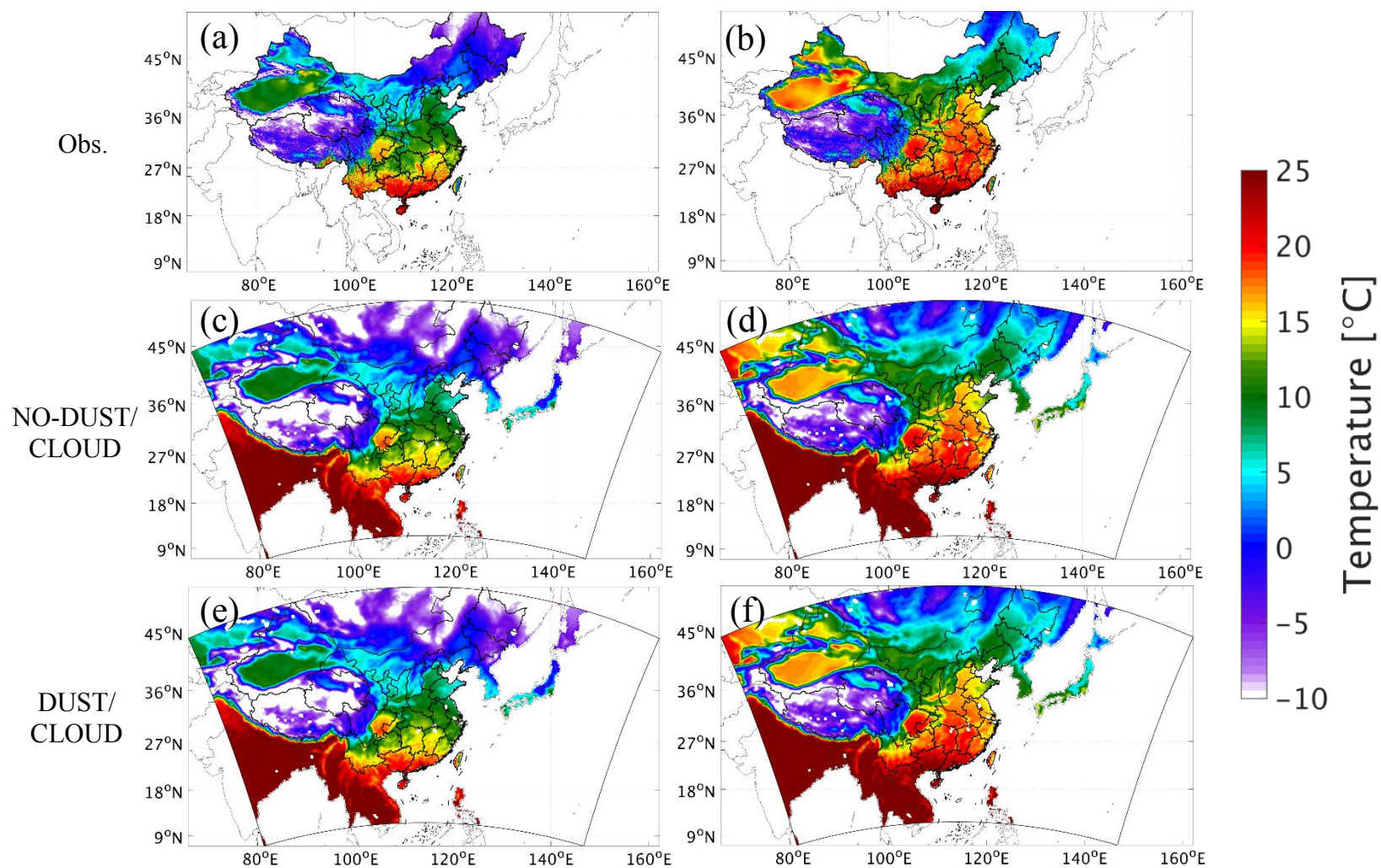
Figure 3: Spatial distributions of the average near-surface temperature from observations (a, b), from NO-DUST/CLOUD (c, d), and from DUST-CLOUD (e, f) during March (left panel) and April (right panel) 2012.
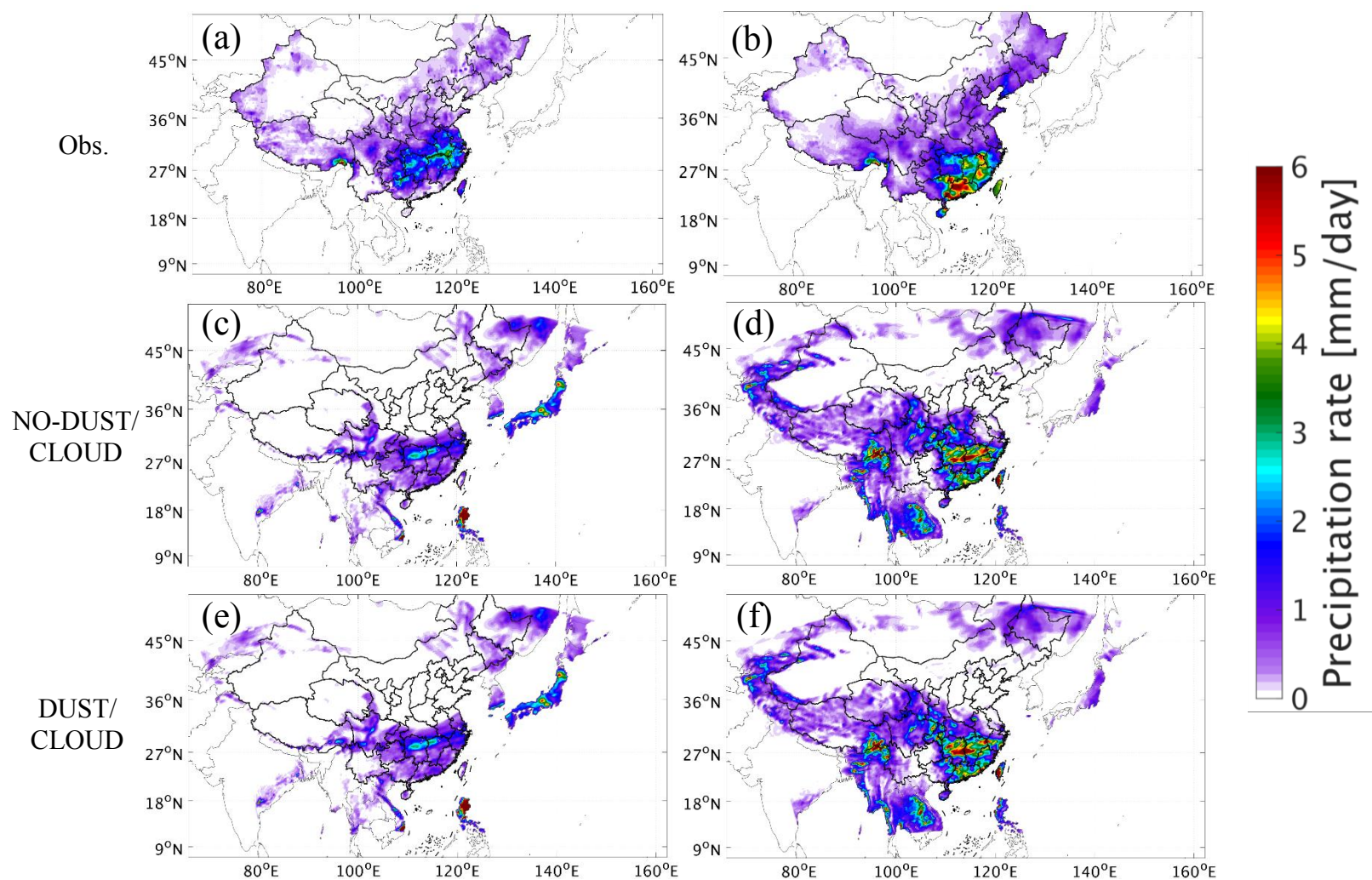
Figure 4: Spatial distributions of the average precipitation rate from observations (a, b), from NO-DUST/CLOUD (c, d), and from DUST/CLOUD (e, f) during March (left panel) and April (right panel) 2012.
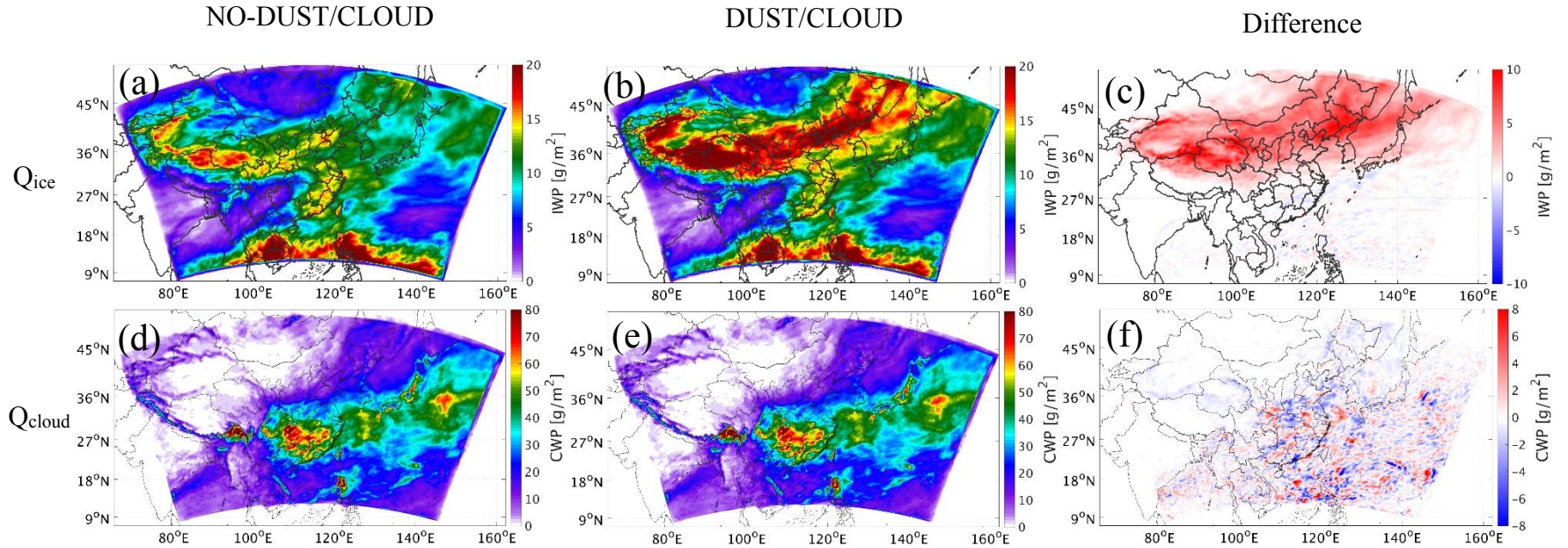
Figure 5: Spatial distributions of the average simulated IWP (a-c) and CWP (d-f) from NO-DUST/CLOUD (left panel), DUST/CLOUD (middle panel), and difference between DUST/CLOUD and NO-DUST/CLOUD (right panel).
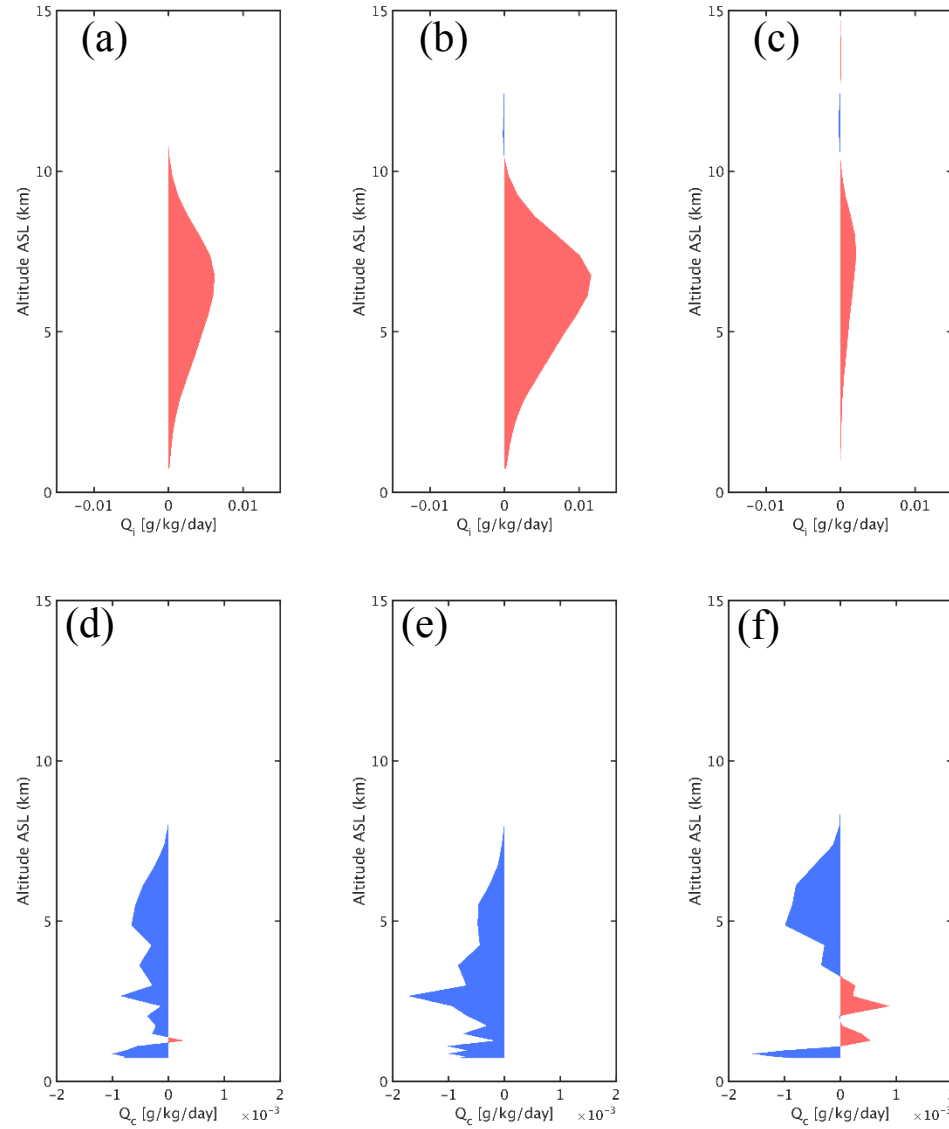
Figure 6: Vertical profile of the modification of cloud ice (a-c) and cloud water content (e-f) induced by dust over the entire simulation domain (left panel), over land (middle panel), and over ocean (right panel).
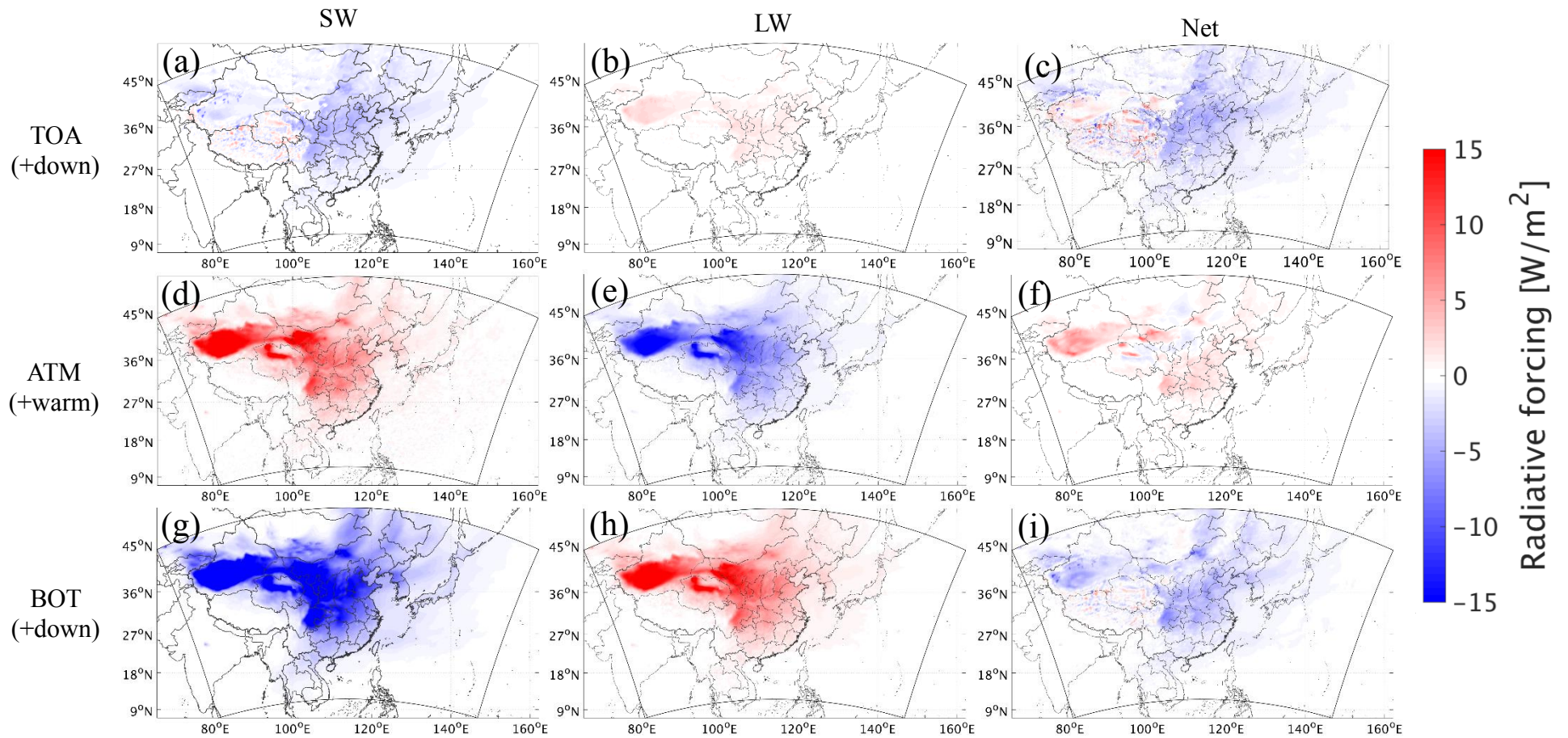
Figure 7: Spatial distributions of the clear-sky SW (left panel), LW (middle panel), and net (right panel) radiative forcing at the top of the atmosphere (TOA, a-c), within the atmosphere (ATM, d-f), and at the bottom of the atmosphere (BOT, g-i).
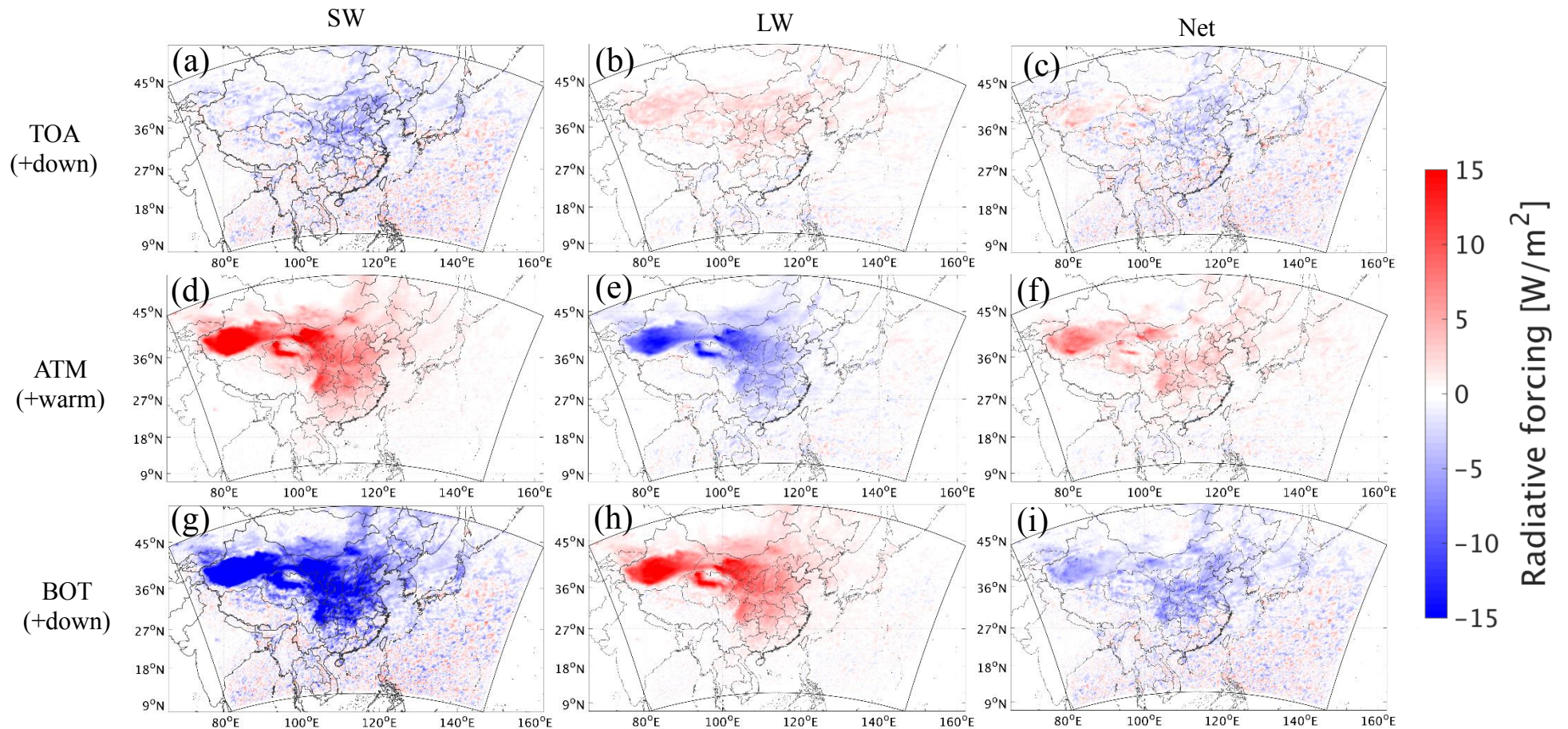
Figure 8: Spatial distributions of the all-sky SW (left panel), LW (middle panel), and net (right panel) radiative forcing at the top of the atmosphere (TOA, a-c), within the atmosphere (ATM, d-f), and at the bottom of the atmosphere (BOT, g-i).
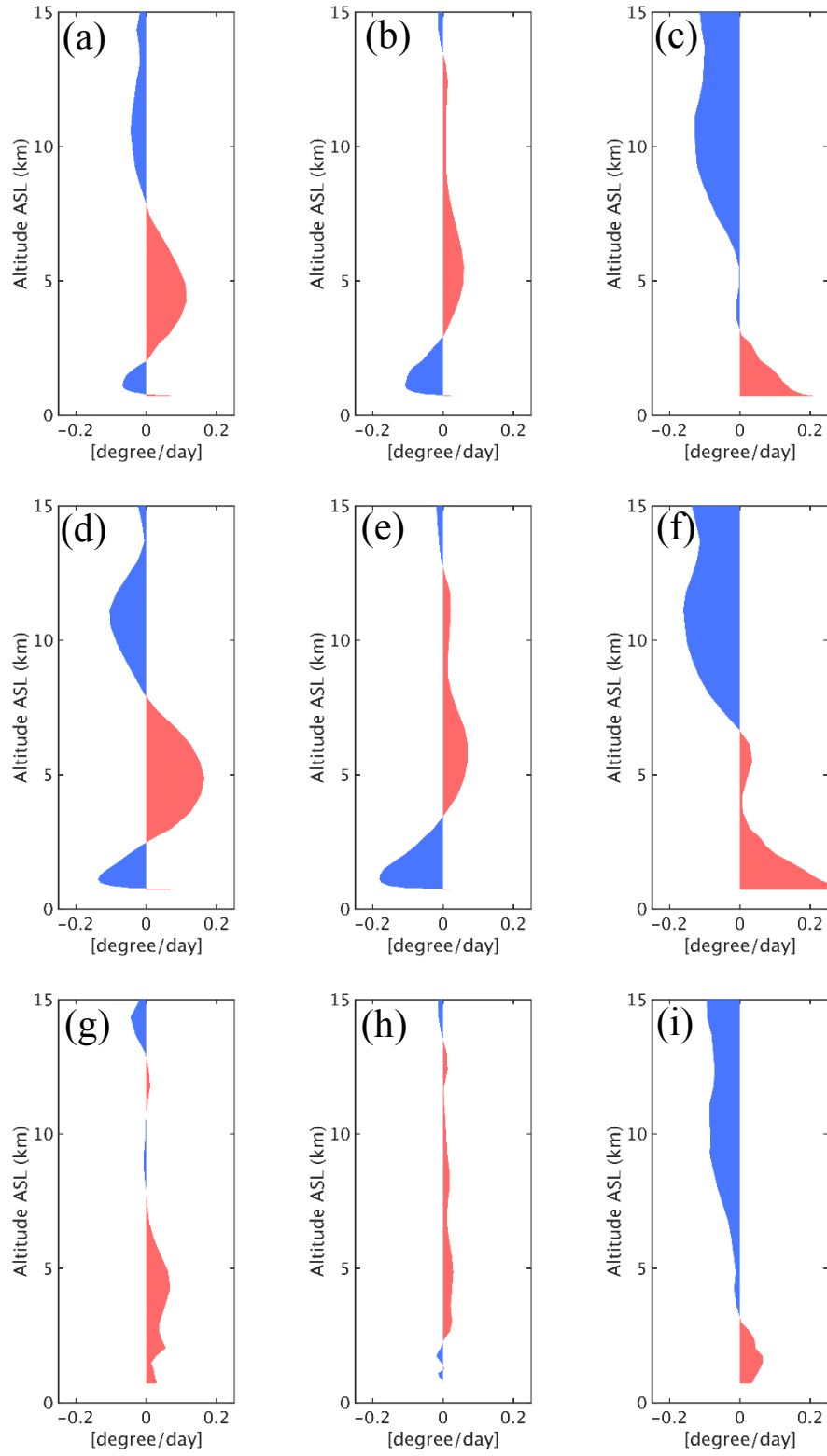
Figure 9: Modification of vertical temperature profile induced by the full effects of dust (left panel), the direct radiative effect of dust (middle panel), and the semi-direct and indirect effects of dust (right panel) over the entire simulation domain (a-c), over land (d-f), and over ocean (g-i).
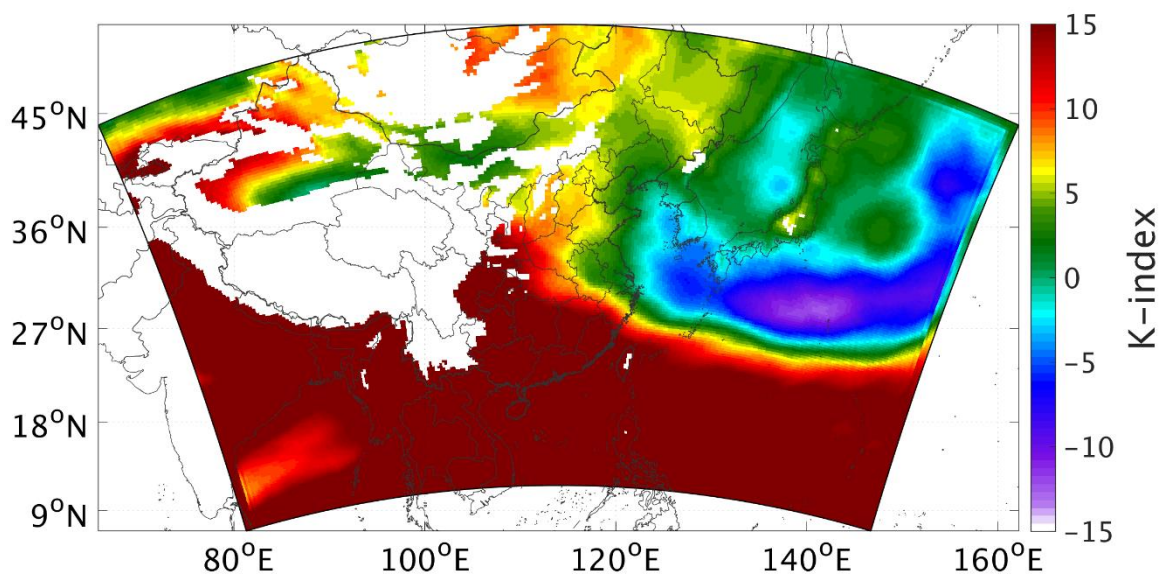
Figure 10: Spatial distributions of the monthly average K-index from NO-DUST/CLOUD.
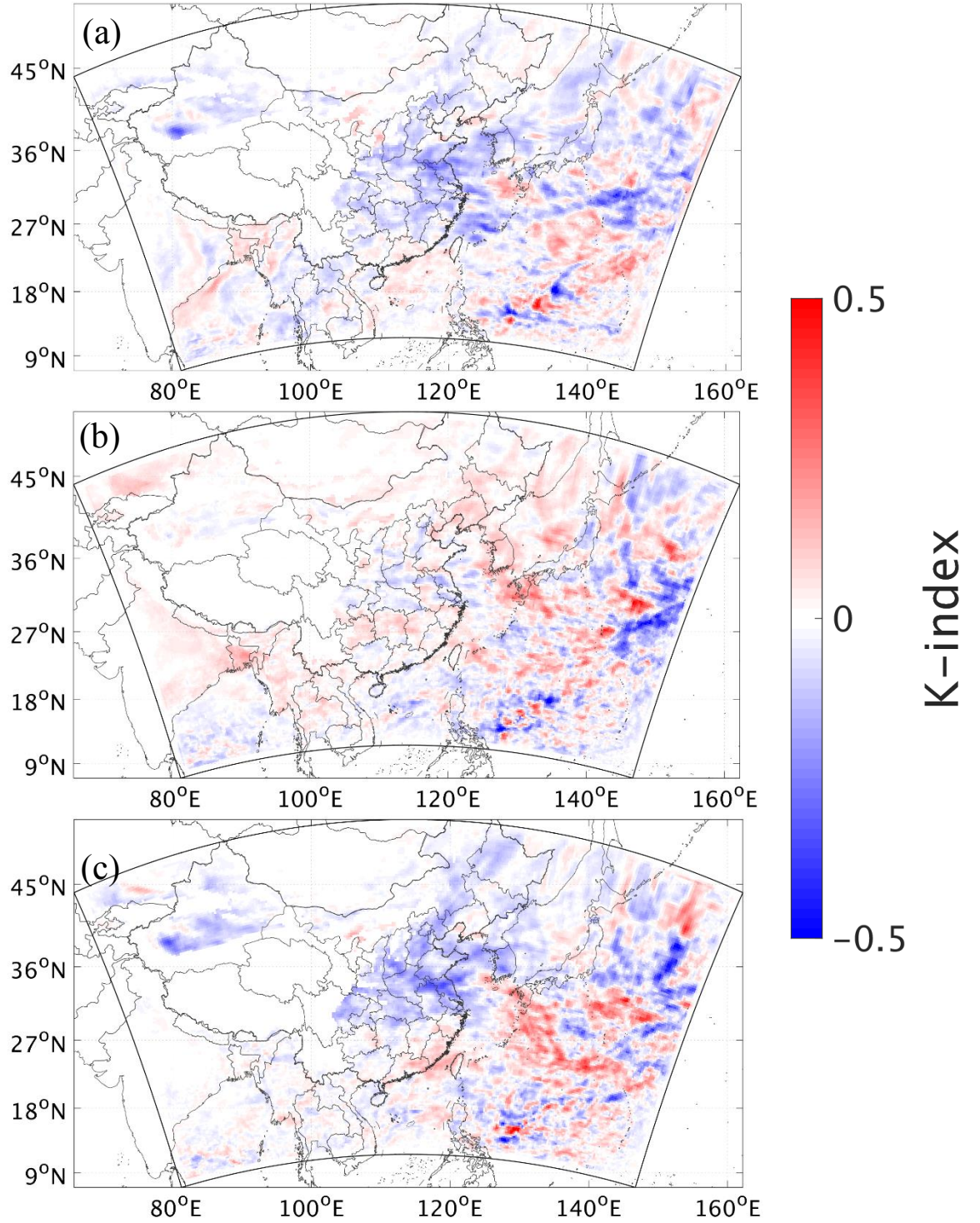
Figure 11: Spatial distributions of the modification of K-index induced by the direct radiative effect of dust (a), the semi-direct and indirect effects of dust (b), and the full effects of dust (c).
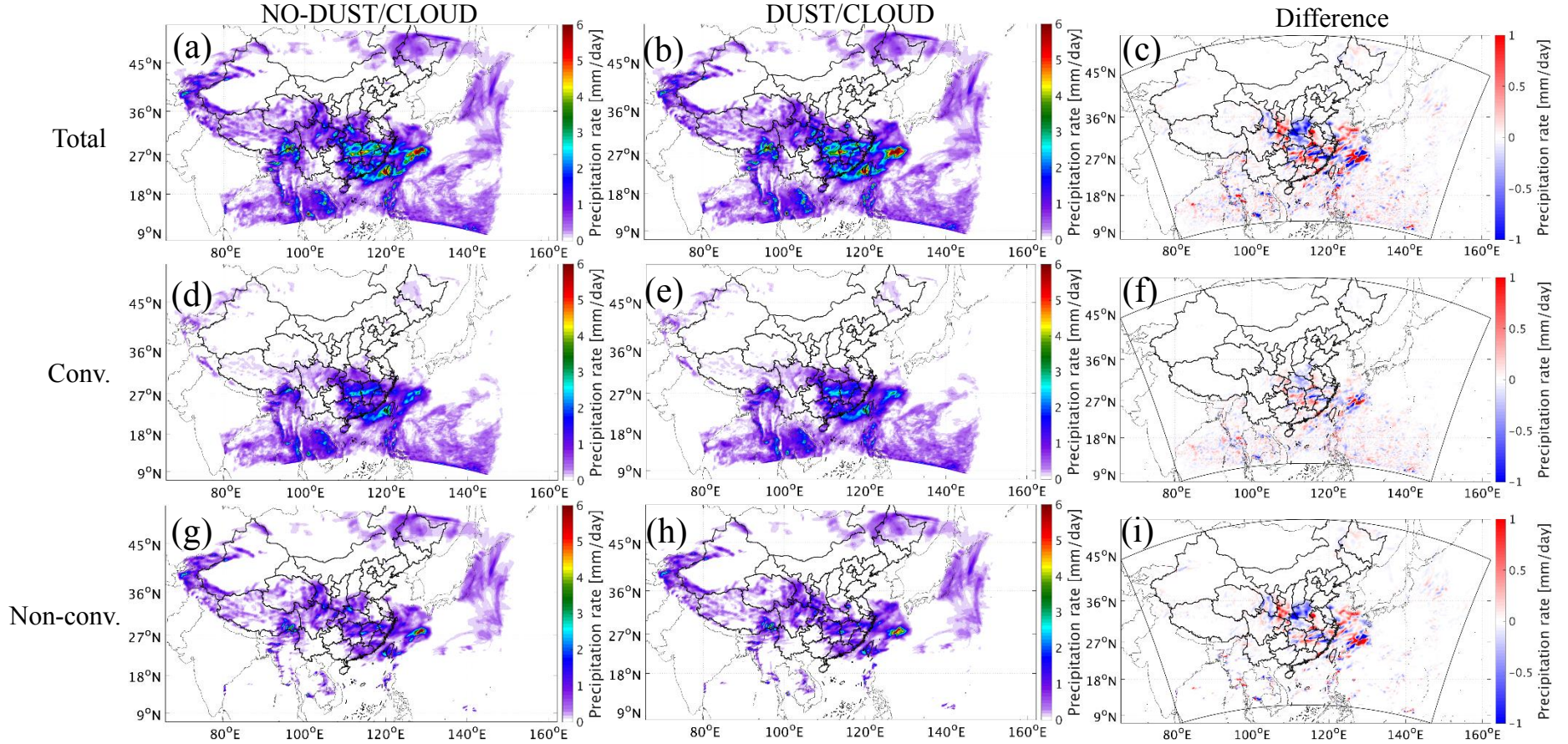
Figure 12: Spatial distributions of the average simulated total precipitation rate (a-c), convective precipitation rate (d-f), and non-convective precipitation rate (g-i) from NO-DUST/CLOUD (left panel), DUST/CLOUD (middle panel), and the difference between DUST/CLOUD and NO-DUST/CLOUD (right panel).